

# Single-pulse studies of three millisecond pulsars

Nipuni T. Palliyaguru,<sup>1</sup>★ B. B. P. Perera,<sup>2</sup> M. A. McLaughlin,<sup>3,4</sup> S. Osłowski,<sup>5</sup> and G. L. Siebert<sup>6</sup>

<sup>1</sup> Department of Physics and Astronomy, Texas Tech University, Lubbock, TX 79409, USA

<sup>2</sup> Arecibo Observatory, University of Central Florida, HC3 Box 53995, Arecibo, PR 00612, USA

<sup>3</sup> Department of Physics and Astronomy, West Virginia University, Morgantown, WV 26501, USA

<sup>4</sup> Center for Gravitational Waves and Cosmology, West Virginia University, Chestnut Ridge Research Building, Morgantown, WV 26505, USA

<sup>5</sup> Manly Astrophysics, 15/41-42 East Esplanade, Manly, NSW 2095, Australia

<sup>6</sup> Department of Physics, University of Wisconsin Madison, Madison, WI 53703, USA

Accepted XXX. Received YYY; in original form ZZZ

## ABSTRACT

Single-pulse studies are important to understand the pulsar emission mechanism and the noise floor in precision timing. We study total intensity and polarimetry properties of three bright millisecond pulsars – PSRs J1022+1001, J1713+0747, and B1855+09 – that have detectable single pulses at multiple frequencies. We report for the first time the detection of single pulses from PSR J1022+1001 and PSR J1713+0747 at 4.5 GHz. In addition, for those two pulsars the fraction of linear polarization in the average profile is significantly reduced at 4.5 GHz, compared to 1.38 GHz, which could support the expected deviation from a dipolar field closer to the pulsar surface. While the fraction of linear polarization in single pulses of PSR J1022+1001 also follows this trend, the few single pulses in our data set of J1713+0747 seem to show a higher fraction of linear polarization at 4.5 GHz than at 1.38 GHz. We do not find evidence for orthogonal modes in single pulses for any of the pulsars. More sensitive multi-frequency observations may be useful to confirm these findings. The jitter noise contributions at 1.38 GHz, scaled to one hour, for PSR J1022+1001 and PSR J1713+0747 are  $\approx 220$  ns and  $\approx 41$  ns respectively and are consistent with previous studies, but for B1855+09 the jitter noise is  $\approx 86$  ns, which is lower than previously measured. We also show that selective bright-pulse timing of PSR J1022+1001 yields improved root-mean-square residuals of  $\approx 23$   $\mu$ s, which is a factor of  $\approx 4$  better than timing using single pulses alone.

**Key words:** stars: neutron – pulsars: general – pulsars: individual: PSR J1022+1001, J1713+0747, B1855+09

## 1 INTRODUCTION

In general, pulsar emission remains poorly understood. The commonly accepted model suggests that emission is produced by curvature radiation from bunches of charged particles moving along magnetic field lines at relativistic speeds. The emitted photons split into electron-positron pairs, producing a cascade of secondary pair plasma (Goldreich & Julian 1969; Ruderman & Sutherland 1975). Components of the electric field that are parallel ( $E_{\parallel}$ ) and perpendicular ( $E_{\perp}$ ) to the magnetic field lines produce highly linearly polarized emission. Circular polarization is thought to be generated both by intrinsic mechanisms and/or by propagation effects within the magnetosphere (Melrose 1995), where a time delay is introduced between  $E_{\parallel}$  and  $E_{\perp}$  due to different refractive indices of the two orthogonal components in the magnetosphere (Gil & Snakowski 1990). As the pulsar beam crosses our line of sight, sweeping through different magnetic field lines, the polarization position angle (PPA), which is the angle between the magnetic field line and the fiducial plane (i.e., the plane passing through the rotation and magnetic axes) makes an S-shaped curve (Radhakrishnan & Cooke 1969). The PPA infor-

mation is utilized in constraining the geometry of pulsars using the rotating vector model (e.g. Rankin 1983a,b; Mitra & Rankin 2011).

However, pulsar emission is extremely complex, requiring sophisticated models and many observations exist that do not fit into this general picture. For example, even though average profiles are stable, emission is highly variable at a single-pulse level. Some pulsars show giant pulses (Heiles & Campbell 1970), mode changing (Backer 1970), drifting sub-pulses (Drake & Craft 1968; Backer 1973), nulling (Rankin 1986) and microstructure within single pulses (Cordes et al. 1990) which are not easily explained by a simple emission model. The PPA of some pulsars deviate from the S-shaped sweep and show discontinuities and rapid jumps. These are sometimes separated by  $90^{\circ}$ , named orthogonal polarization modes (OPMs), and may result from either two highly polarized orthogonal modes of emission (e.g. Backer et al. 1976; Cordes et al. 1978) or propagation effects (McKinnon & Stinebring 2000). Even though the curvature radiation with bunches explains the radio emission of pulsars to some extent, it has serious drawbacks, including the inability to explain the production of bunches and their existence over the characteristic time of emission (Melrose 1992). Furthermore, secondary pair plasma is insufficient to reach the charge density required by Maxwell’s equations (e.g. Melrose 1995). As alternative

★ E-mail: nipuni.palliyaguru@ttu.edu

mechanisms, relativistic plasma emission, anomalous Doppler emission, linear acceleration emission, and maser emission have been proposed. However, none of these theoretical methods are capable of fully explaining the pulsar emission mechanism (Melrose 1995; Melrose et al. 2021). Therefore, single-pulse studies, including single-pulse-polarimetry, of pulsars with a variety of properties are crucial to fully understand pulsar emission physics (Rankin 1986).

Millisecond pulsars (MSPs) are old neutron stars that are spun up to millisecond periods. They have smaller magnetospheres and relatively smaller (~four orders of magnitude) magnetic field strengths than canonical pulsars, which have not been through the recycling process (Lorimer & Kramer 2012). This poses the question of whether emission of MSPs is different from canonical pulsars. For example, the emission beam size of a canonical pulsar is correlated with its period but such a correlation cannot be clearly seen for MSPs (Kramer et al. 1998). In addition, MSP profiles appear to show less evolution with frequency than those of canonical pulsars (Kramer et al. 1998). Some properties of canonical and millisecond pulsars are similar, however. For instance, MSPs can emit giant pulses, like normal pulsars; there is evidence that giant pulses are linked to high magnetic-field strengths at the pulsar light cylinder and to high-energy emission (Romani & Johnston 2001; Enoto et al. 2021). MSPs too may show a deviation from the dipolar field line structure close to the NS surface (e.g. Kramer et al. 1998; Gil et al. 2002; Kalapotharakos et al. 2021).

Furthermore, millisecond pulsars (MSPs) are important for low-frequency, from nHz to  $\mu$ Hz, gravitational wave detection experiments through pulsar timing arrays (PTAs), which require precise measurements of pulse times of arrival (TOAs) and sub-microsecond timing accuracy (Alam et al. 2021; Desvignes et al. 2016; Kerr et al. 2020; Perera et al. 2019, 2018). Pulse-to-pulse jitter, profile variations, variation in polarization properties, and polarization calibration errors are among phenomena that could affect the precision of TOAs (Cordes & Shannon 2010). These can contribute to noise that can limit the timing precision of MSPs and therefore sensitivity of PTAs to gravitational waves. Therefore studying MSPs at a single-pulse level to understand the contributions of these various phenomena can offer useful insights.

Single-pulse studies of MSPs have been sparse due to signal-to-noise ratio limitations due to their low fluxes (Kramer et al. 1998) and data acquisition requirements such as the need for high time resolution sampling. The few previous studies have revealed highly linearly polarized single pulses and sub-pulse microstructure in J0437–4715 (Jenet et al. 1998; Osłowski et al. 2014), giant pulses from B1937+21 (Jenet et al. 2001), pulse jittering from PSR J1713+0747 (Shannon & Cordes 2012) and PSR J1022+1001 (Liu et al. 2015; Feng et al. 2020), and sub-pulse drifting from PSR J1713+0747 (Liu et al. 2015).

Polarization information in single pulses could get lost when averaging, causing depolarization in averaged pulse profiles (Backer, & Rankin 1980). Therefore studying single pulses may provide clues to the emission physics of pulsars. In addition to emission mechanisms, there are other advantages to performing polarimetry. Britton (2000) suggested the possibility of using invariant profiles to avoid errors due to calibration and van Straten (2006) suggested the use of polarimetric profiles to improve timing. Furthermore, Osłowski et al. (2013) used polarization information to correct for pulse-to-pulse variability in PSR J0437–4715, which resulted in a 40% improvement in the timing precision of the pulsar. In light of these ideas, we investigate single-pulse emission properties in three stable millisecond pulsars – PSR J1022+1001, PSR J1713+0747, and PSR B1855+09 – which are monitored regularly by PTAs (see Perera

**Table 1.** Properties of the observed pulsars: The pulsar period, period derivative, the dispersion measure, and references.

Name	Period (ms)	$\dot{P}$ ( $s\ s^{-1}$ )	DM ( $cm^{-3}\ pc$ )	Reference
J1022+1001	16.453	$4.334 \times 10^{-20}$	10.252	1,2
J1713+0747	4.570	$8.530 \times 10^{-21}$	15.917	3,4
B1855+09	5.362	$1.784 \times 10^{-20}$	13.314	4

References: (1) Hotan et al. (2006), (2) Reardon et al. (2016), (3) Zhu et al. (2015), (4) Arzoumanian et al. (2018).

et al. 2019). PSR J1022+1001 is known to show long-term profile instabilities (e.g. Kramer et al. 1999; Padmanabh et al. 2021) and PSR J1713+0747 recently underwent a significant pulse shape change (e.g. Xu et al. 2021). While the origin of such changes is likely intrinsic, and not due to incorrect calibration, these events can introduce variations in timing residuals, degrading the PTA sensitivity to gravitational waves.

The paper is structured as follows. The details of observations and data processing are presented in Section 2. Data analysis techniques are presented in Section 3 and results are presented in Section 4. The summary and conclusion of the study are presented in Section 5.

## 2 OBSERVATIONS AND DATA PROCESSING

PSRs J1022+1001, J1713+0747, and B1855+09 were observed with the 305-m William E. Gordon Telescope at the Arecibo observatory in Puerto Rico. The basic parameters of these three millisecond pulsars<sup>1</sup> are given in Table 1. Arecibo observations were carried out between August 5, 2018 and August 25, 2019. Data were recorded using the Puerto Rico Ultimate Pulsar Processing Instrument (PUPPI) at center frequencies of 430 MHz, 1380 MHz, 2030 MHz and 4500 MHz in full Stokes mode with 8-bit sampling. Our multi-frequency observation details, including the usable bandwidth, number of channels across the usable bandwidth and the sampling time, for each pulsar, are listed in Table 2. The usable bandwidth at 1.38 GHz and 2.3 GHz is less than the full receiver bandwidth due to radio frequency interference (RFI). While baseband recording mode allows higher time resolution, we accumulated data in search mode in order to maximize the available bandwidth and thereby to improve the S/N of the pulsar data. PSRs J1713+0747 and B1855+09 data were coherently dedispersed using DSPSR<sup>2</sup> (van Straten & Bailes 2011) at the dispersion measure listed in Table 2. PSR J1022+1001 was observed in the incoherent search mode. Each observation session started with a noise calibrator injection scan followed by the pulsar observation.

The recorded data were processed with DSPSR (van Straten & Bailes 2011) to obtain single pulses, which were further processed with PSRCHIVE<sup>3</sup> routines (Hotan et al. 2004). The data from each pulsar were processed with 512 pulse phase bins given the time resolution used in the observation setup. The automatic median zapping algorithms of PSRCHIVE were used to remove narrow-band and impulsive RFI. Remaining RFI was removed by visual inspection.

Polarization calibration was performed to correct for the differential gain and phase between the two polarization channels of the

<sup>1</sup> <https://www.atnf.csiro.au/research/pulsar/psrcat/>

<sup>2</sup> <http://dspsr.sourceforge.net>

<sup>3</sup> <http://psrchive.sourceforge.net>

receiver due to imperfections in the amplifiers and mismatch between the cable chains along the two paths, assuming an ideal feed. For this, we used the calibrator scan which is a 25 Hz winking cal signal which ideally injects a fully linearly polarized signal in between the two polarization probes at a 45° position angle. Next, the instrumental response was determined using polarization calibration modeling (pcm) as outlined in Britton (2000), assuming equal ellipticities of receptors. A flux calibrator was not observed during these observations. The polarization properties of the integrated profiles are shown in Figure 1, which are consistent with previously published profiles (Dai et al. 2015).

Faraday rotation due to the magnetized ISM and the ionosphere causes a change in the PPA with frequency (e.g. Simard-Normandin & Kronberg 1980; Lyne & Smith 1989). The change in the PPA due to Faraday rotation is given by

$$\Delta\Psi = \lambda^2 \times \text{RM}, \quad (1)$$

where  $\lambda$  is the observation wavelength. The rotation measure (RM), which depends on the average magnetic field and the electron density along the line-of-sight, was calculated using the `rmfit` program in `PSRCHIVE`, which searches for a peak in the linear polarization for trial RMs. The best-fit RM values (published values in parenthesis) are given in Table 2. Given the  $\lambda^2$  dependence in Equation 1, and the decrease in flux density with increasing frequency, the sensitivity to the change in the PPA decreases with increasing frequency. Therefore, the RM values derived from 1.38 GHz data were used to correct the data at higher frequencies.

Our RM values at 1.38 GHz are consistent within errors with published values for MSPs J1713+0747 and B1855+09 (see Table 2). However, significant trends in the measured RM has been observed for PSR J1713+0747 previously (Wahl et al. 2021). Our measured RM for PSR J1022+1001 differs significantly from its published value, however, PSR J1022+1001 is known to show changes in the RM when passing close to the sun i.e. when the angular separation between the pulsar and the sun is  $< 3^\circ$  (You et al. 2012) and also shows significant long-term RM variations (Yan et al. 2011). The angular separation between the sun and the pulsar was  $\approx 15^\circ$  during the 1.38 GHz observations. While it is not possible to pinpoint to the reason for the discrepancy between our measured and previously published RM values for PSR J1022+1001, we note that Noutsos et al. (2015) and Feng et al. (2020) also find higher RM values of 2.18(2) rad m<sup>-2</sup> and 2.9(2) rad m<sup>-2</sup> respectively.

For the pulse phase jitter analysis, average profiles of 50, 100, 200, 500, and 1000 pulses were created. A TOA for each profile was generated by cross-correlating it against a noise-free template profile. This template was obtained by fitting Gaussian components to a high S/N profile obtained by averaging over the full observation for a given frequency. Timing residuals were obtained using the `TEMPO2` pulsar timing package (Edwards et al. 2006; Hobbs et al. 2006). The timing ephemerides are obtained from data published in Perera et al. (2019).

### 3 DATA ANALYSIS

In this section we discuss total intensity properties, polarimetry of single pulses, and pulse phase jitter of PSRs J1022+1001, J1713+0747, and B1855+09.

Table 2 lists the measured equivalent pulse width  $W_{eq}$  and the measured flux density  $S_{mean}$  of the average profile over the full observation length from our multi-frequency observations.  $W_{eq}$  is defined as the width of a top hat pulse with the peak amplitude

$I_{peak}$  and the same area as the on-pulse region and is calculated as

$$W_{eq} = \frac{\sum_{i=n_1}^N I_i}{I_{peak}}, \quad (2)$$

where  $I_i$  is the intensity of the  $i^{th}$  bin of the on-pulse region ranging from bins  $n_1$  to  $N$  in baseline-corrected data. The error of  $W_{eq}$  is calculated by applying error propagation on Equation 2 and using the off-pulse rms as the error of  $I_i$ .

From the radiometer equation, the root mean square noise fluctuation is given by

$$\Delta S_{sys} = \frac{T_{sys}}{G \sqrt{N_p t_{obs} \Delta\nu}} = C \sigma_p. \quad (3)$$

Here,  $C$  is the scaling factor,  $\sigma_p$  is the standard deviation of the off-pulse region,  $T_{sys}$  is the system temperature, which is the sum of the sky temperature ( $T_{sky}$ ), the receiver temperature ( $T_{rec}$ ), and the telescope spill over,  $G$  is the telescope gain,  $\Delta\nu$  is the bandwidth,  $t_{obs}$  is the observation length, and  $N_p = 2$  is the number of polarization channels (see Lorimer & Kramer 2012). The measured mean flux density  $S_{mean}$  is calculated by scaling the profile by  $C$  (i.e.  $\Delta S_{sys}/\sigma_p$ ). The values for  $T_{rec}$ ,  $T_{sky}$ , and  $G$  for different frequencies are listed in Table 2.

#### 3.1 Single-pulse properties

We analyze single-pulse properties of the five data sets. Figure 1 shows a single-pulse sequence (a stack of individual pulses in time vs pulse-phase), the total intensity and polarization profiles (see Section 3.2 for polarimetry) of averaged data and the three highest S/N individual single pulses from each data set.

Single-pulse amplitude and S/N distributions are used to identify phenomena such as giant pulses, which have flux density  $> 10\times$  the mean flux density (Karuppusamy et al. 2012; Knight 2007). Figure 2 shows the histograms of peak pulse amplitude distribution and the S/N distribution of single pulses of PSRs J1022+1001, J1713+0747, and B1855+09 at frequencies 1.38 GHz and 4.5 GHz. The S/N for each single-pulse is calculated as

$$S/N = \frac{I_{peak}}{\sigma_p} \quad (4)$$

where  $I_{peak}$  is the peak amplitude, and  $\sigma_p$  is the off-pulse standard deviation of the pulse profile. The number and the fraction of detected single pulses ( $S/N > 5$ ) is listed in Table 2. Figure 3 shows the single-pulse equivalent width vs S/N.

#### 3.2 Single-pulse polarimetry

Stokes parameters I, Q, U, V describe the polarization of electromagnetic waves, such that I is the total intensity, Q and U describe the intensity of linear polarization L as  $L = \sqrt{Q^2 + U^2}$ , and V is the intensity of circular polarization (see Lorimer & Kramer 2012). The polarization position angle is defined as  $\text{PPA} = 0.5 \tan^{-1}(U/Q)$ . Figure 4 shows the histograms of single-pulse linear and circular polarization fraction at the peak. Table 3 lists the linear and circular polarization fraction of the average profiles and the peak of the distributions of single-pulse polarization fractions shown in Figure 4. The error on the polarization fraction of the average profile are obtained by using the standard deviation of I, L, and V across the profile and applying error propagation. The peak of the histogram and the error are obtained from the best fit Gaussian profile of the histogram.

**Table 2.** Observation information, including MJD, frequency, observation length, bandwidth, number of channels across the bandwidth, sampling time, receiver temperature, sky temperature, measured rotation measures (published rotation measures are given in parentheses), equivalent width, measured mean flux density from the radiometer equation, and the number (and fraction) of pulses detected ( $S/N > 5\sigma$ ).

Name	MJD	$\nu$ (MHz)	Length (s)	BW (MHz)	$N_{\text{chan}}$	G K/Jy	$t_{\text{samp}}$ ( $\mu\text{s}$ )	$T_{\text{rec}}$ (K)	$T_{\text{sky}}$ (K)	RM ( $\text{rad m}^{-2}$ )	$W_{\text{eq}}$ (ms)	$S_{\text{mean}}$ (mJy)	N
J1022+1001	58335	1380	300	600	384	8	20.48	30	0.62	$5.31 \pm 0.04$ (−0.3, 2.18)	$1.028 \pm 0.002$	$4.89 \pm 0.04$	10755 ( $\approx 59\%$ )
	58651	4500	1800	800	512	4	40.96	30	0.03	$-59.36 \pm 21.88$	$0.577 \pm 0.003$	$0.90 \pm 0.02$	1175 ( $\approx 1\%$ )
J1713+0747	58697	1380	300	600	384	8	10.24	30	2.92	$10.69 \pm 0.04$ (13 $\pm$ 2)	$0.1752 \pm 0.0003$	$10.18 \pm 0.03$	64458 ( $\approx 98\%$ )
	58697	4500	300	800	512	4	10.24	30	0.14	$-47.55 \pm 24.64$	$0.195 \pm 0.002$	$1.37 \pm 0.04$	53 ( $\approx 0.08\%$ )
B1855+09	58720	430	600	20	64	11	2.56	50	109.9	–	$0.53 \pm 0.01$	$10.61 \pm 0.75$	–
	58720	1380	1200	600	384	8	10.24	30	5.11	$24.99 \pm 0.18$ (20 $\pm$ 4)	$0.483 \pm 0.001$	$5.21 \pm 0.03$	11480 ( $\approx 10\%$ )
	58720	2030	600	460	384	8	10.24	40	1.94	$-8.04 \pm 2.4$	$0.43 \pm 0.02$	$0.39 \pm 0.05$	–

Notes:

The published RM values are obtained from Yan et al. (2011), Noutsos et al. (2015) and Gentile et al. (2018).

The RM of PSR B1855+09 is not calculated at 430 MHz due to the small bandwidth.

$T_{\text{rec}}$  and Gain values for AO are obtained from <http://www.naic.edu/~astro/RXstatus/rcvrtabz.shtml>.

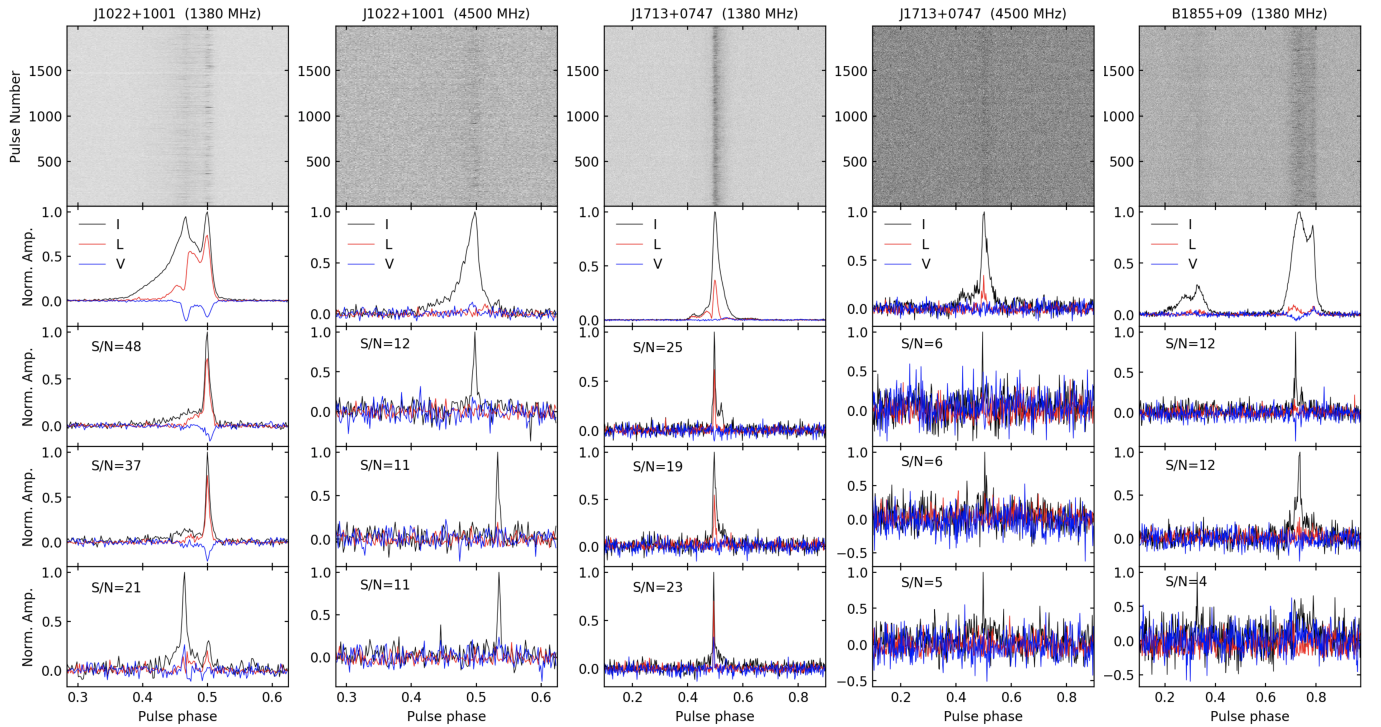


**Figure 1.** Multi-frequency single pulse observations of PSRs J1022+1001, J1713+0747, and B1855+09 at observing frequency 1.38 and 4.5 GHz (see different columns). For each pulsar at each frequency, a sequence of 2000 single pulses in grey scale (*top panel*) and the averaged profiles, including total intensity (*black*), linear (*red*) and circular (*blue*) polarization (*second panel from top*) are shown. Three highest S/N single-pulse profiles are shown from each observation (*bottom three panels*). A single pulse associated with the leading component of PSR J1022+1001 at 1.4 GHz with a low fraction of linear polarization is also shown. Two single pulses of PSR J1022+1001 at 4.5 GHz which appear at the small trailing component at phase  $\approx 0.53$  (away from the main component) are also shown.

Phase resolved histograms of the PPA for single-pulse data were obtained using `psrspa` routine in `PSRCHIVE`. Figure 5 shows the logarithm distribution of single-pulse PPA as a function of pulse phase along with the PPA of the average profile. The histogram is weighted by the total intensity.

### 3.3 Pulse phase jitter

As demonstrated by Shannon & Cordes (2012), timing residuals due to pulse-to-pulse jitter are expected to be correlated across radio frequency. For average profiles formed with  $N$  pulses, the root-mean-square (rms) residuals due to jitter noise,  $\sigma_J(N)$ , is quantified as the quadrature difference between the measured rms timing residuals,  $\sigma_{\text{obs}}(N)$ , and the expected rms timing residuals from radiometer

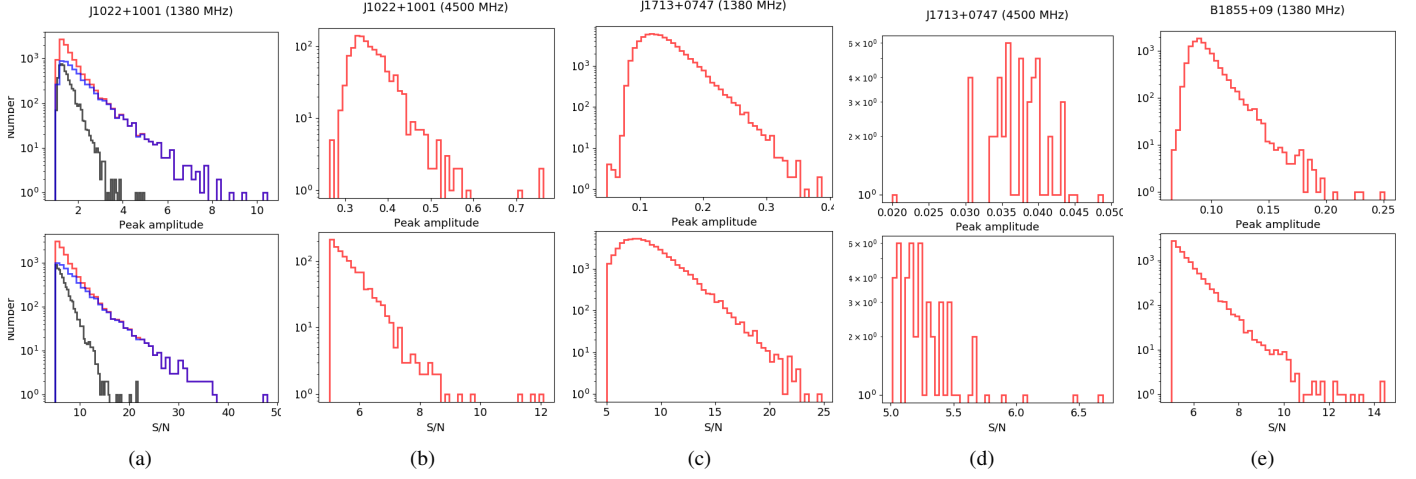


**Figure 2.** Histograms of peak amplitude (top) and S/N (bottom) of PSR J1022+1001 at 1.4 GHz (a) and 4.5 GHz (b), PSR J1713+0747 at 1.4 GHz (c), and 4.5 GHz (d), and PSR B1855+09 at 1.4 GHz (e). For PSR J1022+1001 at 1.4 GHz, the histograms of single-pulses associated with the leading (black) and trailing (blue) components are also shown separately in addition to the histograms of all single pulses (red). The brightest seem to correspond to the trailing component.

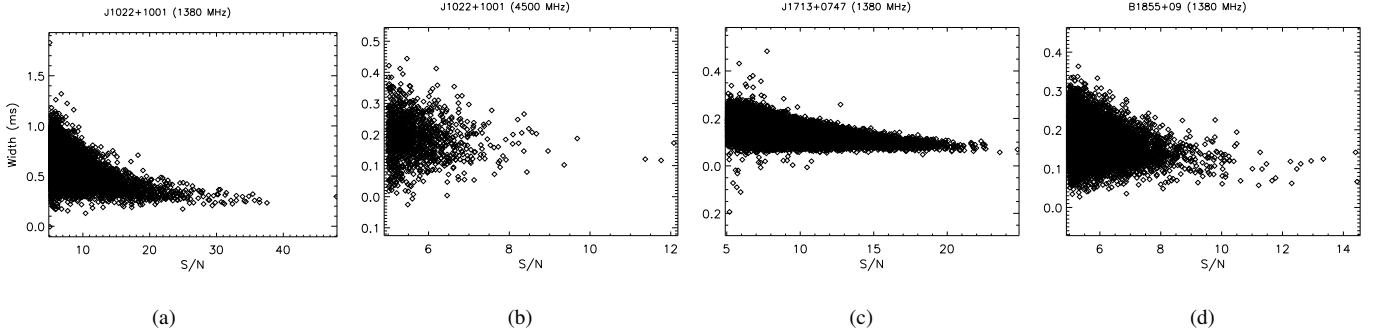


**Figure 3.** Measured single-pulse equivalent width and S/N values for PSR J1022+1001 at 1.4 GHz (a) and 4.5 GHz (b), PSR J1713+0747 at 1.4 GHz (c), and PSR B1855+09 at 1.4 GHz (d). Widths of J1713+0747 single pulses at 4.5 GHz are not shown due to the small fraction of detected pulses with S/N>5.

**Table 3.** Polarization parameters: percentage fractional linear and circular polarization of the average profile and the peak of the histograms of linear and circular polarizations shown in Figure 4.

Pulsar	Frequency (MHz)	$L_{av}/I_{av}$	$V_{av}/I_{av}$	L/I	V/I
J1022+1001	1380	$73.9 \pm 0.2$	$-18.0 \pm 0.2$	$27.3 \pm 1.1$ , $70.8 \pm 0.3$	$-13.2 \pm 0.2$
J1022+1001	4500	$3.2 \pm 0.3$	$6.9 \pm 0.4$	$21.8 \pm 0.7$	$7.3 \pm 0.6$
J1713+0747	1380	$36.6 \pm 0.5$	$0.9 \pm 0.5$	$36.3 \pm 0.1$	$0.6 \pm 0.1$
J1713+0747	4500	$30.1 \pm 0.6$	$-1.4 \pm 0.8$	$39.8 \pm 0.2$	$-6.7 \pm 3.2$
B1855+09	1380	$6.6 \pm 0.1$	$-3.5 \pm 0.2$	$26.3 \pm 0.3$	$-2.2 \pm 0.1$

For J1022+1001 at 1.4 GHz the peak fractional linear polarization for leading and trailing components are listed separately.

noise only,  $\sigma_{rad}(N)$ , such that (Shannon & Cordes 2012)

$$\sigma_J(N)^2 = \sigma_{obs}(N)^2 - \sigma_{rad}(N)^2. \quad (5)$$

In order to determine the effect of jitter, composite profiles were formed with  $N = 50, 100, 200, 500,$  and  $1000$  pulses averaged together. For these various  $N$  values,  $\sigma_{obs}(N)$  was calculated from the timing residuals of the measured TOAs (obtained as described in Section 2) and  $\sigma_{rad}(N)$  was calculated from simulated profiles of

similar S/N levels as the observed single pulses. The simulated profiles were constructed by adding white noise to a noise-free template with signal-to-noise drawn from the signal-to-noise distribution of the observed single pulses. We note that the simulated dataset does not contain uncertainties due to profile shape variations or any other phenomena. The rms residuals due to jitter noise were determined from Equation 5 for various  $N$  values. The rms residuals due to jitter for one hour averages were determined from the parameters of the

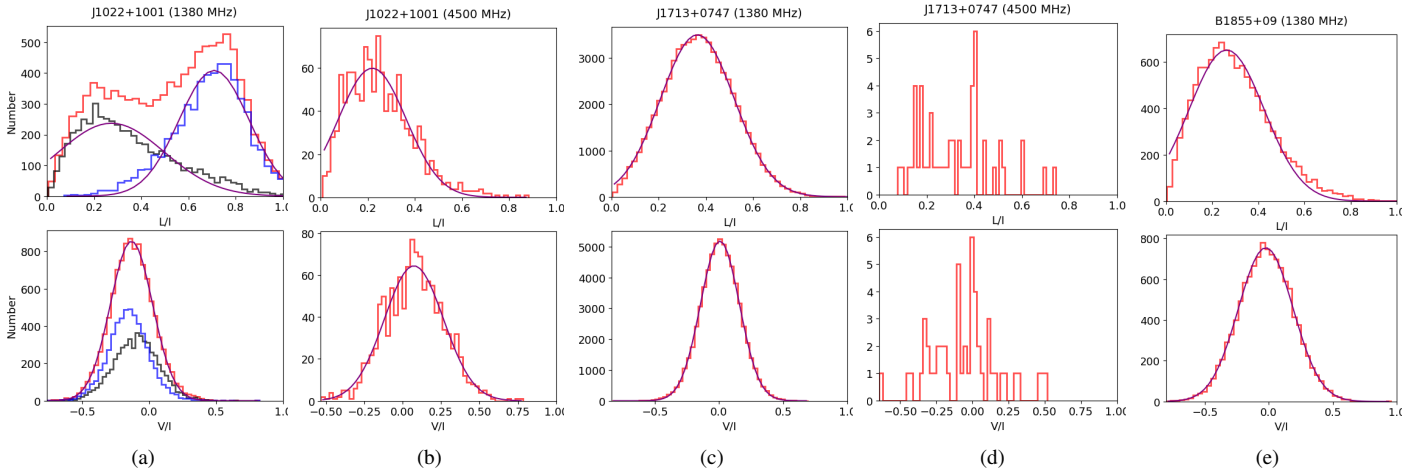


**Figure 4.** Histograms of linear polarization (red) and the Gaussian fit (purple) for PSR J1022+1001 at 1.4 GHz (a) and 4.5 GHz (b), PSR J1713+0747 at 1.4 GHz (c), and 4.5 GHz (d), and PSR B1855+09 at 1.4 GHz (e). For PSR J1022+1001 at 1.4 GHz, the histograms of single-pulses associated with the leading (black) and trailing (blue) components are also shown separately with their respective Gaussian fits. Single pulses associated with the trailing component show a higher fractional linear polarization than those associated with the leading component. The Gaussian fit for 4.5 GHz data of J1713+0747 is not shown due to the limited number of pulses.

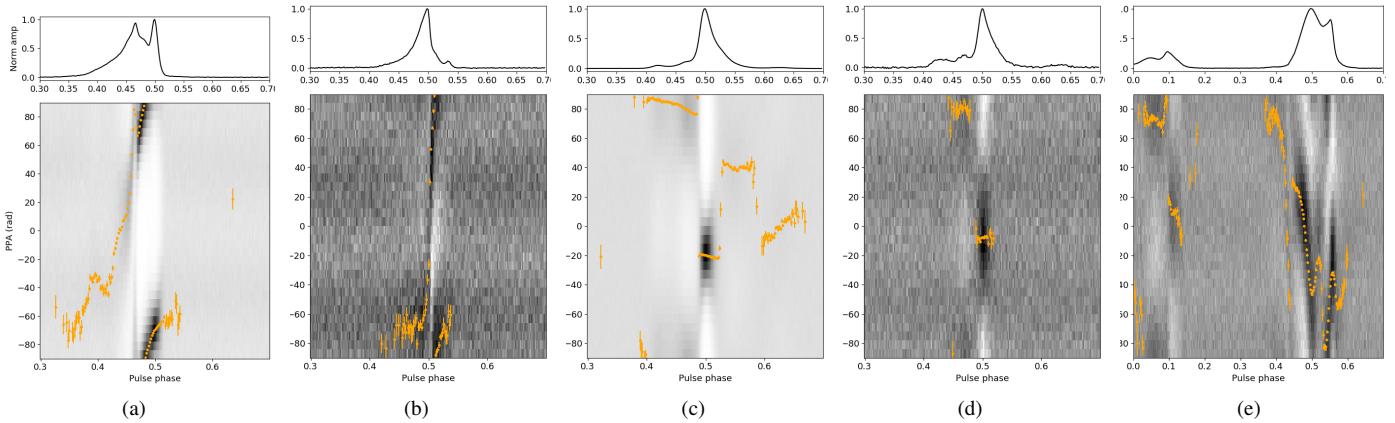


**Figure 5.** The total intensity average profile (top) and the single-pulse PPA distribution (bottom grey scale) of for PSR J1022+1001 at 1.4 GHz (a) and 4.5 GHz (b), PSR J1713+0747 at 1.4 GHz (c), and 4.5 GHz (d), and PSR B1855+09 at 1.4 GHz (e). The PPA of the average profile (orange) is also marked.

best-fit line to  $\sigma_J(N)$  vs  $N$  such that  $\sigma_J(N) = AN^\beta$ , as shown in the bottom panel of Figure 6.

Timing residuals due to jitter noise are correlated between subbands. The band may be split into several subbands and the correlation may be calculated between adjacent subbands (Parthasarathy et al. 2021). Following Shannon & Cordes (2012), we calculate the rms due to jitter by correlating timing residuals from the top and bottom halves of the band as  $\sigma_j = \sqrt{\text{CCF}(0)}$ . Here,  $\text{CCF}(0)$  is the zero-lag value of the cross-correlation function.

To calculate the cross-correlation, the full bandwidth was divided into two subbands and TOAs were generated for each subband separately. A different template profile was used for each subband. Then the timing residuals were calculated for each band. Figure 6 shows the correlation between the timing residuals from the top and bottom halves of the band, for 1000-pulse averages, along with the best-fit line whose slope should be ideally be unity. The slopes of the best-fit lines for the three pulsars are listed in Table 4. Table 4 also lists the zero lag value of the cross-correlation function  $\text{CCF}(0)$ , rms timing

residuals  $\sigma_{\text{obs}}$  for 1000-pulse averages, the TOA error from radiometer noise  $\sigma_{\text{rad}}$ , rms residuals due to jitter calculated from Equation 5, the best-fit parameters of the line  $\sigma_J(N)$  vs  $N$ , and rms residuals due to jitter, from Equation 5, scaled to one hour using the best-fit parameters. The error on the jitter level scaled to one hour is obtained by applying error propagation to  $\sigma_J(N) = AN^\beta$ .

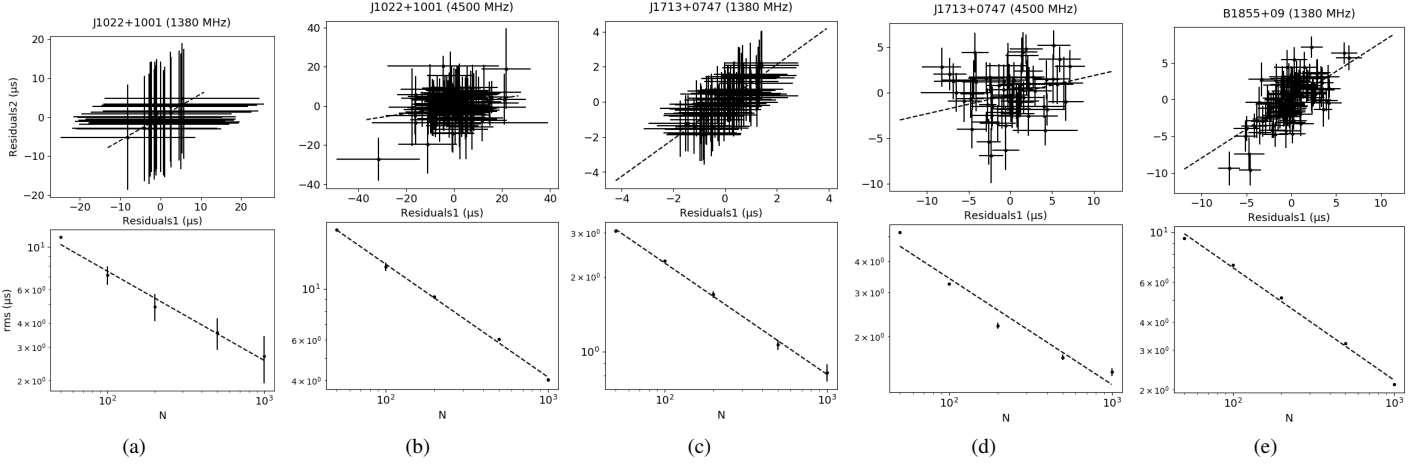


**Figure 6.** Correlation between TOAs of top and bottom halves of the band for 1000-pulse averages along with the best-fit line (top), and the rms timing residuals from jitter vs the number of pulses averaged (bottom) for PSR J1022+1001 at 1.4 GHz (a) and 4.5 GHz (b), PSR J1713+0747 at 1.4 GHz (c), and 4.5 GHz (d), and PSR B1855+09 at 1.4 GHz (e). In the bottom plots the best-fit line to jitter noise is shown by the dashed line. The correlation is negligible for both PSRs J1022+1001 and J1713+0747 at 4.5 GHz for 1000-pulse averages likely due to radiometer noise in profiles.

**Table 4.** Phase jitter analysis: Pulsar name, frequency, the slope of the best fit to the timing residual correlation for 1000-pulse averages ( $m$  - see the top panel of Figure 6), the corresponding zero-lag value of the CCF (CCF(0)), rms residuals due to jitter from the CCF ( $\sigma_{j,CCF}$ ), measured rms timing residuals ( $\sigma_{obs}$ ), rms residuals due to radiometer noise ( $\sigma_{rad}$ ), rms residuals due to jitter ( $\sigma_j$ ) from the quadrature difference between  $\sigma_{obs}$  and  $\sigma_{rad}$ , jitter scaling parameters ( $A, \beta$  - see text), and  $\sigma_j$  scaled to one hour ( $\sigma_{j,1hr}$ ).

Pulsar	Frequency (MHz)	$m$	CCF(0) ( $\mu s^2$ )	$\sigma_{j,CCF}$ (ns)	$\sigma_{obs}$ (ns)	$\sigma_{rad}$ (ns)	$\sigma_j$ (ns)	( $A, \beta$ )	$\sigma_{j,1hr}$ (ns)
J1022+1001	1380	0.68	0.86	929	2844	718	2752	(61.97, -0.46)	220±46
J1022+1001	4500	0.24	0.28	528	5302	3422	4049	(120.8, -0.49)	301±22
J1713+0747	1380	1.04	0.85	924	835	107	829	(17.75, -0.44)	41±3
J1713+0747	4500	0.11	0.15	382	2204	1655	1456	(23.70, -0.42)	78±24
B1855+09	1380	0.80	0.56	747	2308	912	2120	(69.56, -0.49)	86±9

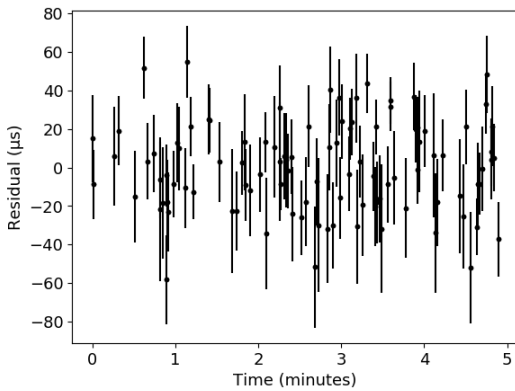


**Figure 7.** The rms timing residuals of PSR J1022+1001 single-pulses of  $S/N > 25$  at 1.4 GHz.

## 4 RESULTS AND DISCUSSION

Single pulses of  $S/N > 5$  are detected for PSRs J1022+1001 and J1713+0747 at 1.38 GHz and 4.5 GHz, and for B1855+09 at 1.38 GHz. The 2.3 GHz data set of B1855+09 does not show detectable single pulses. To the best of our knowledge, this is the first

report of the detection of single pulses at frequencies  $> 2$  GHz in MSPs. Below, we discuss each pulsar individually.

### 4.1 PSR J1022+1001

As shown in Figure 1, PSR J1022+1001 shows a double-peaked profile with a highly linearly polarized ( $\approx 74\%$ ) trailing component at 1.4 GHz, as also noted previously (Hotan et al. 2004; Liu et al. 2015). At 4.5 GHz the profile changes to a single component, which is only  $\sim 3\%$  linearly polarized. The percentage of circular polarization remains negligible at both 1.38 GHz and 4.5 GHz. This pulsar shows long-term profile variations (Kramer et al. 1999), which have been attributed to improper polarization calibration (van Straten 2013). By using the measured flux densities given in Table 2, we measure a spectral index of  $-1.43 \pm 0.04$ , slightly lower than the published value of  $-1.7 \pm 0.1$  (Kramer et al. 1998). The rms timing residuals due to pulse-to-pulse jitter at 1.38 GHz, scaled to one hour, is  $220 \pm 46$  ns. This is consistent (within the  $2\text{-}\sigma$  error) with the Shannon et al. (2014) value of  $290 \pm 15$  ns and  $269 \pm 4$  ns of Lam et al. (2019) but higher than the  $67 \pm 9$  ns and  $269 \pm 4$  ns reported by Feng et al. (2020) or  $\approx 700$  ns for 1-min integration ( $\approx 90$  ns for one hour) reported by Liu et al. (2015) at 1.38 GHz. The level of jitter at 4.5 GHz, scaled to one hour, is  $301 \pm 22$  ns, which is higher than that at 1.38 GHz.

Following Liu et al. (2015) and Feng et al. (2020), we measured the rms timing residuals of single pulses from the leading and trailing component separately. Considering all single pulses with  $S/N > 5$  results in rms timing residuals of  $\approx 74 \mu\text{s}$  and  $\approx 48 \mu\text{s}$  for leading and trailing components respectively. For TOA calculation, the template profile was created by averaging over all pulses of  $S/N > 5$  within each component. Liu et al. (2015) finds rms timing residuals of  $4.3 \mu\text{s}$  for averages of 30 trailing component sub-pulses of  $S/N > 5$ , which converts to  $4.3 \times \sqrt{30} \approx 23 \mu\text{s}$  at the single-pulse level. The reason for higher rms timing residuals in our dataset could be the higher levels of jitter compared to Liu et al. (2015) possibly due to the pulsar showing variable jitter noise.

We also measured the rms timing residuals of single pulses within  $S/N$  ranges of  $5 < S/N < 15$ ,  $15 < S/N < 25$  and  $S/N > 25$ . As shown in Figure 7, the rms timing residual using the brightest pulses ( $S/N > 25$ ) is  $\approx 23 \mu\text{s}$ . For TOA calculation, the template profile was created by averaging over all pulses within each  $S/N$  range. Scaling the rms of  $\approx 2.8 \mu\text{s}$  from 1000-pulse averages (Table 4) simply as  $\sigma_{obs} \propto 1/\sqrt{N_p}$  (e.g. Shannon & Cordes 2012), where  $N_p$  is the number of pulses in the average profile, the expected single-pulse RMS is  $\approx 89 \mu\text{s}$ . So timing just the brightest pulses gives a factor of  $\approx 4$  improvement. The vast majority of pulses (99%) within  $S/N > 25$  range appear at the leading component. Using single pulses within the  $S/N$  ranges of  $5 < S/N < 15$  and  $15 < S/N < 25$  yields rms timing residuals of 77 and 106  $\mu\text{s}$  respectively. The higher rms residuals in pulses within the  $15 < S/N < 25$  range could be due to a small percentage (3.7%) of pulses occurring at the trailing component while the rest occur at the leading component. When these trailing edge pulses are removed, the rms timing residuals within  $15 < S/N < 25$  reduce to 36  $\mu\text{s}$ .

We do not see evidence for giant pulses. However, the data set consists of very bright pulses of ( $S/N \approx 30$ ), which are  $\approx \times 5$  the mean  $S/N$ . At 4.5 GHz, some bright single pulses appear at phase  $\approx 0.53$  (phase  $\approx 0.03$  away from the main component) as shown in Figure 1. Overall, single pulses with the higher  $S/N$  seem to be narrower than the ones with smaller  $S/N$  at 1.38 GHz, as shown in Figure 3. Generally, at low  $S/N$ , the true width may be difficult to measure resulting in large width estimates. However, we note that  $W_{eq}$  measured here may not be affected by noise in profiles. We find that the single-pulse linear polarization distribution of PSR J1022+1001 at 1.38 GHz shows two peaks (see Figure 4). Single pulses associated with the leading component of the average profile tend to have a low linear polarization fraction (average  $L/I \approx 0.3$ ) compared to the single pulses associated with the second peak (average  $L/I \approx 0.7$ ). As evident from Table 3 and Figure 4, in general, the fraction of linear polarization is reduced at higher frequencies. Single pulses at 4.5 GHz show higher fractional  $L/I$  compared to the average profile.

The PPA of the average profile follows an S-shaped swing with a "notch" at the first peak (Figure 4(a)) as also reported by Kramer et al. (1999). The brightest single pulses of J1022+1001 at 1.38 GHz are highly linearly polarized, as also noted in other studies (Liu et al. 2015).

## 4.2 PSR J1713+0747

PSR J1713+0747 is a binary pulsar which shows relativistic effects (Camilo et al. 1994; Splaver et al. 2005). PSR J1713+0747 shows a multi-component average profile with a significant linear polarization ( $\approx 37\%$ ) at the peak at 1.38 GHz, consistent with previous studies (e.g. Yan et al. 2011). This is reduced but still significant ( $\approx 30\%$ ) at 4.5 GHz. We measure a spectral index of  $-1.69 \pm 0.06$  using the flux densities obtained at 1.38 GHz and 4.5 GHz (see Ta-

ble 2), which is consistent (within the  $2\sigma$  error) with the published value of  $-1.5 \pm 0.1$  (Kramer et al. 1998). The more prominent outer components at 4.5 GHz compared to at 1.38 GHz (at phases  $\approx 0.42$  and 0.47), also reported in Kijak et al. (1997), are evident in our data (see Figure 1). The faint emission component at phase  $\approx 0.63$  at 1.4 GHz is also more prominent at 4.5 GHz. Previous studies have reported a jitter contribution of  $\approx 35 \pm 0.8$  ns to rms timing residuals in one hour of integration of this pulsar (Shannon et al. 2014; Liu et al. 2016), consistent (within the  $2\sigma$  error) with the  $41 \pm 3$  ns that we find at 1.38 GHz. The level of pulse-to-pulse jitter for this pulsar at 4.5 GHz, scaled to one hour, is  $78 \pm 24$  ns, which is higher than at 1.38 GHz.

Although, the data set consists of very bright pulses of  $S/N \approx 20$ , we do not see evidence for giant pulses. Overall, single pulses with the higher  $S/N$  seems to be narrower than the ones with smaller  $S/N$  at 1.38 GHz, as shown in Figure 3. The fraction of single pulses detected at 4.5 GHz is very small, which stops us from performing detailed analysis.

The PPA of the average profile shows  $90^\circ$  jumps (see Figure 5) that indicate the presence of OPMs (Xilouris et al. 1998). Indeed OPMs have been detected in this pulsar at 1.38 GHz in Large European Array for Pulsars (LEAP) data (Liu et al. 2016). However, there is no sufficient evidence for OPMs in the PPA distribution of single pulses in Figure 5.

## 4.3 PSR B1855+09

PSR B1855+09 is a relativistic binary which has both main pulse (MP) and an interpulse (IP), with both showing a double-peaked structure and weak ( $\approx 7\%$  and  $\approx 2\%$  in the MP and IP respectively) linear polarization consistent with previous studies (Kramer et al. 1998). The PPA of the average profile in the MP does not follow an S-shaped swing. The discontinuities in the PPA curve of the IP is non-orthogonal and consistent with (Xilouris et al. 1998) even though some studies have noted orthogonal transitions (Yan et al. 2011). Based on the measured flux densities at 430 MHz, 1.38 GHz and 2 GHz, we measure a spectral index of  $-0.8 \pm 0.1$ , slightly flatter than the published value of  $-1.3 \pm 0.2$  (Kramer et al. 1998). The flux density measure at 2 GHz is unusually low, likely due to the very low  $S/N$  of the data set. We also note that our data are only polarization calibrated, and therefore these flux density measurements may not be precise. Also note that the MSP spectral index is not well constrained (Bates et al. 2013; Kuniyoshi et al. 2015). We find that the rms timing residual due to jitter, scaled to one hour, is  $86 \pm 9$  ns ( $69 \pm 7 \mu\text{s}$  at the single-pulse level). This is less than the published values obtained for various models in Lam et al. (2019), i.e. single-pulse rms of  $\approx 115.8 \pm 1.3 \mu\text{s}$  and  $105.6^{+3.1}_{-5.2} \mu\text{s}$  for models with and without frequency dependence respectively.

Single pulses of PSR B1855+09 at 1.38 GHz also show higher fractional  $L/I$  compared to the average profile. We also note that even though the flux density at 430 MHz is high, the expected  $S/N$  of a single pulse is low and therefore single pulses are not detected at these low frequencies possibly due to the high sky temperature. For Arecibo observations (parameters listed in Table 2), the expected  $S/N$ , for B1855+09 at 430 MHz, calculated from the radiometer equation,

$$S/N = \frac{G\sqrt{N_p W \Delta\nu} S_{peak}}{T_{sys}} \quad (6)$$

is  $< 5$ . Here  $S_{peak}$  is the peak flux density (estimated using the mean flux density and duty cycle) and we assume that the single-pulse width

is  $W \approx 0.17$  ms, which is the mean single-pulse equivalent width of B1855+09 at 1.38 GHz.

A few single pulses associated with the IP are detected with low S/N (example shown in the bottom panel of Figure 1). However, due to their low S/N, only single-pulses associated with the MP are used for detailed analysis.

## 5 SUMMARY AND CONCLUSION

We have studied the total intensity properties, single-pulse polarimetry and pulse phase jitter of MSPs J1022+1001, J1713+0747, B1855+09 at multiple frequencies. On the single-pulse front, we do not detect giant pulses, but we still find bright single pulses at 1.38 GHz for all three MSPs. Overall, single pulses with higher S/N seems to be narrower than the ones with smaller S/N at 1.38 GHz, as shown in Figure 3.

As evident from Table 3, in general, the fraction of linear polarization in the average profile is reduced at higher frequencies. This may be consistent with similar findings of normal pulsars that show that average profiles are depolarized at higher frequencies (e.g. Xilouris et al. 1996; Johnston et al. 2006). This is because high frequency emission arises closer to the pulsar surface where the magnetic field deviates from a dipole field resulting in superposition of modes and hence significant depolarization (e.g. McKinnon 1997; Wang et al. 2015; van Straten & Tiburzi 2017). Dai et al. (2015) reported this trend for MSPs PSR J1022+1001, PSR J1713+0747 and PSR B1855+09 using 1.38 GHz and 3 GHz observations. Our results confirm that this trend continues at 4.5 GHz for PSR J1022+1001 and PSR J1713+0747. Single pulses from PSR J1022+1001 at 4.5 GHz and PSR B1855+09 at 1.4 GHz show high fractional linear polarization than the average profile, likely due to depolarization from averaging.

In our data set the fraction of single pulses detected at 4.5 GHz is very small, which prevents us from performing detailed analysis. Sensitive observations are needed to better understand single-pulse phenomena at higher frequencies. For example, the expected S/N at 4.5 GHz for a FAST-like telescope (even though FAST cannot observe at frequencies  $> 2$  GHz with current system), with a gain of  $G = 18$  K/Jy,  $T_{\text{sys}} = 20$  K,  $BW = 800$  MHz (Li & Pan 2016), would be a factor of  $\approx 6$  better than our data. Upcoming facilities with high sensitivity and frequency coverage should facilitate multi-frequency single-pulse studies of pulsars.

Comparing the jitter level from the cross-correlation method and quadrature difference between the observed simulated rms timing residuals ( $\sigma_{j,\text{CCF}}$  and  $\sigma_j$  in Table 4),  $\sigma_{j,\text{CCF}}$  seems to be less than  $\sigma_j$  except for PSR J1713+0747 at 4.5 GHz. This could be because jitter is decorrelated across the band (e.g. Parthasarathy et al. 2021). The jitter levels ( $\sigma_j$ ) we find are consistent for PSRs J1022+1002 (Shannon et al. 2014; Lam et al. 2019) and J1713+0747 (Shannon et al. 2014; Liu et al. 2016) at 1.4 GHz, but high for PSR B1855+09 (Lam et al. 2019) at 1.4 GHz compared to previous studies. But the fact that PSR J1022+1001 has lower values of jitter recorded in other studies (Liu et al. 2015; Feng et al. 2020; Parthasarathy et al. 2021) could indicate variable jitter noise. The contribution to the pulsar noise budget from jitter for PSR J1022+1001 and PSR J1713+0747 is higher at 4.5 GHz than at 1.38 GHz. Jitter noise is expected to be lower at higher frequencies due to narrower profiles and lower flux densities, though previous studies have shown that not all pulsars follow this trend (Shannon et al. 2014; Lam et al. 2019). While some MSPs used in PTAs show levels of jitter as low as tens of ns per hour, others (which have large pulse widths and small periods) show levels

of jitter amounting to hundreds of ns per hour (Shannon et al. 2014; Parthasarathy et al. 2021). Lam et al. (2019) has found that 43 pulsars out of a sample of 48 shows significant jitter and that 30 of those show significant frequency dependence. The general notion is that jitter noise should be detectable in all MSPs if observed with adequate sensitivity (Shannon et al. 2014), and therefore accurately including jitter in noise modeling is important in high-precision pulsar timing.

We also find that timing only the brightest pulses of PSR J1022+1001 results in an improvement in rms timing residuals by a factor of  $\approx 4$  than what is expected by timing all single pulses. Therefore the timing precision of this pulsar may be improved if integrated profiles that are used to generate TOAs are created by including only the brightest pulses. We note that previous studies have found that selective timing does not yield a significant improvement in timing (Osłowski et al. 2014; Feng et al. 2020). The first of these studies reported reduced  $\chi^2$  of the timing residuals when selectively integrating only weaker pulses, as well as a minor improvement to timing when using brighter pulses. The reason for our improvement in timing could be because we only include the brightest pulses with a large trailing component and remove the pulses that have a large leading component and thereby selecting only the brightest pulses which appear within the narrow phase range of the trailing component. Our very short data set prevents us from timing using integrated profiles of selected bright pulses, but this is an important avenue for further exploration. Therefore, further investigation is needed to see if selective timing yields an improvement for integrated profiles formed with bright pulses within a given component of the profile.

## DATA AVAILABILITY

The data underlying this article will be shared on reasonable request to the corresponding author.

## ACKNOWLEDGEMENT

The authors thank Hector Hernandez, Phil Perrillat and other Arecibo Observatory staff for help with scheduling, observation support and data quality checks. The Arecibo Observatory is a facility of the National Science Foundation operated under cooperative agreement by the University of Central Florida in alliance with Yang Enterprises, Inc. and Universidad Metropolitana. NP, BPP, and MAM are members of the NANOGRAV Physics Frontiers Center, supported by NSF award #1430284 and #2020265.

## REFERENCES

- Alam, MD F. et al. 2021, ApJS, 252, 4A
- Arzoumanian, Z., Brazier, A., Burke-Spolaor, S., et al. 2018, ApJS, 235, 37. doi:10.3847/1538-4365/aab5b0
- Backer, D. C. 1970, Nature, 228, 1297
- Backer, D. C. 1973, ApJ, 182, 245
- Backer, D. C., Rankin, J. M., & Campbell, D. B. 1976, Nat, 263, 202
- Backer, D. C., & Rankin, J. M. 1980, ApJS, 42, 143
- Bates, S. D., Lorimer, D. R., & Verbiest, J. P. W. 2013, MNRAS, 431, 1352. doi:10.1093/mnras/stt257
- Britton, M. C. 2000, ApJ, 532, 1240
- Cordes, J. M., & Shannon, R. M. 2010, arXiv:1010.3785
- Cordes, J. M., Rankin, J., & Backer, D. C. 1978, ApJ, 223, 961
- Cordes, J. M., Weisberg, J. M., & Hankins, T. H. 1990, AJ, 100, 1882. doi:10.1086/115644

- Dai, S., Hobbs, G., Manchester, R. N., et al. 2015, *MNRAS*, 449, 3223. doi:10.1093/mnras/stv508
- Frake, F. D., & Craft, H. D. 1968, *Nature*, 220, 231
- Desvignes, G. et al. 2016, *MNRAS*, 458, 3341
- Edwards, R. T., Hobbs, G. B., & Manchester, R. N. 2006, *MNRAS*, 372, 1549. doi:10.1111/j.1365-2966.2006.10870.x
- Enoto, T., Terasawa, T., Kisaka, S., et al. 2021, *Science*, 372, 187. doi:10.1126/science.abd4659
- Feng, Y., Hobbs, G., Li, D., et al. 2020, arXiv:2012.06709
- Gentile, P. A., McLaughlin, M. A., Demorest, P. B., et al. 2018, *ApJ*, 862, 47. doi:10.3847/1538-4357/aac9c9
- Gil, J. A., & Snakowski, J. K. 1990, *AAP*, 234, 269
- Gil, J. A., Melikidze, G. I., & Mitra, D. 2002, *A&A*, 388, 235. doi:10.1051/0004-6361:20020473
- Goldreich, P. & Julian, W. H. 1969, *ApJ*, 157, 869. doi:10.1086/150119
- Camilo, F., Foster, R. S., & Wolszczan, A. 1994, *ApJ*, 437, L39. doi:10.1086/187677
- Heiles, C. & Campbell, D. B. 1970, *Nature*, 226, 529. doi:10.1038/226529a0
- Hobbs, G. B., Edwards, R. T., & Manchester, R. N. 2006, *MNRAS*, 369, 655. doi:10.1111/j.1365-2966.2006.10302.x
- Hotan, A. W., Bailes, M., & Ord, S. M. 2004, *MNRAS*, 355, 941. doi:10.1111/j.1365-2966.2004.08376.x
- Hotan, A. W., Bailes, M., & Ord, S. M. 2006, *MNRAS*, 369, 1502. doi:10.1111/j.1365-2966.2006.10394.x
- Hotan, A. W., van Straten, W., & Manchester, R. N. 2004, *PASA*, 21, 302
- Jenet, F. A., Anderson, S. B., Kaspi, V. M., Prince, T. A., & Unwin, S. C. 1998, *ApJ*, 498, 365
- Jenet, F. A., Anderson, S. B., & Prince, T. A. 2001, *ApJ*, 546, 394
- Johnston, S., Karastergiou, A., & Willett, K. 2006, *MNRAS*, 369, 1916. doi:10.1111/j.1365-2966.2006.10440.x
- Kalappotharakos, C., Wadiasingh, Z., Harding, A. K., et al. 2021, *ApJ*, 907, 63. doi:10.3847/1538-4357/abcec0
- Karuppusamy, R., Stappers, B. W., & Lee, K. J. 2012, *A&A*, 538, A7. doi:10.1051/0004-6361/201117667
- Kerr, M. et al. 2020, *PASA*, 37, 20K
- Kijak, J., Kramer, M., Wielebinski, R., et al. 1997, *A&A*, 318, L63
- Knight, H. S. 2007, *MNRAS*, 378, 723. doi:10.1111/j.1365-2966.2007.11810.x
- Kramer, M., Xilouris, K. M., Lorimer, D. R., et al. 1998, *ApJ*, 501, 270
- Kramer, M., Xilouris, K. M., Camilo, F., et al. 1999, *ApJ*, 520, 324. doi:10.1086/307449
- Kuniyoshi, M., Verbiest, J. P. W., Lee, K. J., et al. 2015, *MNRAS*, 453, 828. doi:10.1093/mnras/stv1604
- Lam, M. T., McLaughlin, M. A., Arzoumanian, Z., et al. 2019, *ApJ*, 872, 193. doi:10.3847/1538-4357/ab01cd
- Li, D. & Pan, Z. 2016, *Radio Science*, 51, 1060
- Liu, K., Karuppusamy, R., Lee, K. J., et al. 2015, *MNRAS*, 449, 1158. doi:10.1093/mnras/stv397
- Liu, K., Bassa, C. G., Janssen, G. H., et al. 2016, *MNRAS*, 463, 3239. doi:10.1093/mnras/stw2223
- Lorimer, D. R. & Kramer, M. 2012, *Handbook of Pulsar Astronomy*, by D. R. Lorimer, M. Kramer, Cambridge, UK: Cambridge University Press, 2012
- Lyne, A. G. & Smith, F. G. 1989, *MNRAS*, 237, 533. doi:10.1093/mnras/237.3.533
- Maron, O., Kijak, J., & Wielebinski, R. 2004, *A&A*, 413, L19. doi:10.1051/0004-6361:20031707
- McKinnon, M. M. 1997, *ApJ*, 475, 763. doi:10.1086/303542
- McKinnon, M. M. & Stinebring, D. R. 2000, *ApJ*, 529, 435. doi:10.1086/308264
- Melrose, D. B. 1992, *The Magnetospheric Structure and Emission Mechanisms of Radio Pulsars*, IAU Colloquium 128, 306
- Melrose, D. B. 1995, *Journal of Astrophysics and Astronomy*, 16, 137
- Melrose, D. B., Rafat, M. Z., Mastrano, A. 2021, *MNRAS*, 500, 4530
- Mitra, D. & Rankin, J. M. 2011, *ApJ*, 727, 92
- Noutsos, A., Sobey, C., Kondratiev, V. I., et al. 2015, *A&A*, 576, A62. doi:10.1051/0004-6361/201425186
- Ostrowski, S., van Straten, W., Demorest, P., & Bailes, M. 2013, *MNRAS*, 430, 416
- Ostrowski, S., van Straten, W., Bailes, M., et al. 2014, *MNRAS*, 441, 3148. doi:10.1093/mnras/stu804
- Padmanabh, P. V., Barr, E. D., Champion, D. J., et al. 2021, *MNRAS*, 500, 1178. doi:10.1093/mnras/staa3174
- Parthasarathy, A., Bailes, M., Shannon, R. M., et al. 2021, *MNRAS*, 502, 407. doi:10.1093/mnras/stab037
- Perera, B. B. P. et al. 2018, *MNRAS*, 478, 218
- Perera, B. B. P. et al. 2019, *MNRAS*, 490, 4666
- Radhakrishnan, V. & Cooke, D. J. 1969, *Astrophys. Lett.*, 3, 225
- Rankin, J. M. 1983, *ApJ*, 274, 333
- Rankin, J. M. 1983, *ApJ*, 274, 359
- Rankin, J. M. 1986, *ApJ*, 301, 901. doi:10.1086/163955
- Romani, R. W. & Johnston, S. 2001, *ApJ*, 557, L93. doi:10.1086/323415
- Shannon, R. M., Ostrowski, S., Dai, S., et al. 2014, *MNRAS*, 443, 1463. doi:10.1093/mnras/stu1213
- Splaver, E. M., Nice, D. J., Stairs, I. H., et al. 2005, *ApJ*, 620, 405. doi:10.1086/426804
- Reardon, D. J., Hobbs, G., Coles, W., et al. 2016, *MNRAS*, 455, 1751. doi:10.1093/mnras/stv2395
- Ruderman, M. A. & Sutherland, P. G. 1975, *ApJ*, 196, 51. doi:10.1086/153393
- Shannon, R. M., & Cordes, J. M. 2012, arXiv:1210.7021
- Simard-Normandin, M. & Kronberg, P. P. 1980, *ApJ*, 242, 74. doi:10.1086/158445
- van Straten, W. 2004, *ApJS*, 152, 129
- van Straten, W. 2006, *ApJ*, 642, 1004
- van Straten, W., & Bailes, M. 2011, *PASA*, 28, 1
- van Straten, W. 2013, *ApJS*, 204, 13. doi:10.1088/0067-0049/204/1/13
- van Straten, W., & Tiburzi, C. 2017, *ApJ*, 835, 293. doi:10.3847/1538-4357/835/2/293
- Wahl, H. M., McLaughlin, M., Gentile, P. A., et al. 2021, arXiv:2104.05723
- Wang, P. F., Wang, C., & Han, J. L. 2015, *MNRAS*, 448, 771. doi:10.1093/mnras/stu2765
- Yan, W. M., Manchester, R. N., van Straten, W., et al. 2011, *MNRAS*, 414, 2087. doi:10.1111/j.1365-2966.2011.18522.x
- You, X. P., Coles, W. A., Hobbs, G. B., et al. 2012, *MNRAS*, 422, 1160. doi:10.1111/j.1365-2966.2012.20688.x
- Xilouris, K. M., Kramer, M., Jessner, A., et al. 1996, *A&A*, 309, 481
- Xilouris, K. M., Kramer, M., Jessner, A., et al. 1998, *ApJ*, 501, 286. doi:10.1086/305791
- Xu, H., Huang, Y. X., Burgay, M., et al. 2021, *The Astronomer's Telegram*, 14642
- Zhu, W. W., Stairs, I. H., Demorest, P. B., et al. 2015, *ApJ*, 809, 41. doi:10.1088/0004-637X/809/1/41